Journal of Thermal Analysis and Calorimetry, Vol. 63 (2001) 249–266

MICROCALORIMETRIC EVALUATION OF PRECIPITATION IN Cu–2Be–0.2Mg

E. Donoso and A. Varschavsky

Universidad de Chile, Facultad de Ciencias Físicas y Matemáticas, Instituto de Investigaciones y Ensayes de Materiales, Plaza Ercilla 883, Casilla 1420, Santiago, Chile

(Received April 14, 2000)

Abstract

Beryllium precipitation from the Cu-rich matrix in a Cu–2 mass% Be–0.2 mass% Mg alloy homogenized and quenched from 1073 K was studied by differential scanning calorimetry (DSC). The DSC traces showed two main exothermic effects, A and B, each comprising two subeffects: A_1 and A_2, and B_1 and B_2 respectively. Effects A_1 and A_2 correspond to the precipitation of GP zones and subsequent overlapping and independent precipitation of the γ'' phase. Only at very low heating rates can γ'' be inherited from GP zones. Effects B_1 and B_2 correspond to heat evolved during transitions to the states with γ' and γ phases, respectively. Heat effect A can be quantitatively described in terms of solid solubilities before and after precipitation, and of the precipitation heats of the phases involved. The heat content of the combined GP zone/γ'' phase precipitation effect was proportional to the number of beryllium atoms precipitated, yielding an average value of 21 kJ mol^{-1} beryllium for beryllium precipitation. It was shown that the γ' phase arises from the combined transition from states with GP zones and γ'' phases, whereas γ arises from the transition of states with γ'' and γ' phases. The apparent activation energies associated with GP zones and γ'', γ' and γ phases are 1.16±0.08, 1.18±0.07, 1.37±0.08 and 1.74±0.09 eV, respectively. These values are discussed in terms of the mobility of dissolved atoms related to the concentrations of excess vacancies and solute-vacancy complexes, and the direction of plate-like precipitate growth (either normal or perpendicular to the plate). It is inferred that the main roles of magnesium are to decrease the amount and rate of GP formation, to enhance the volume fraction of γ'' and to suppress the discontinuous precipitation of γ'.

Keywords: beryllium, copper, DSC, magnesium, precipitation

Introduction

The excellent age-hardenability and high electrical conductivity of Cu–Be alloys have been used extensively [1–6], e.g. for springs, diaphragms, bearings and non-sparking tools. In this alloy system, the precipitation sequence from the supersaturated solid solution includes at least four stages [7–10]:

$$\text{solid solution} \rightarrow \text{GP zones} \rightarrow \gamma'' \rightarrow \gamma' \rightarrow \gamma$$

1418–2874/2001/ $ 5.00

Akadémiai Kiadó, Budapest
Kluwer Academic Publishers, Dordrecht

where the GP zones are multilayer plates that form coherently on {100} matrix planes, γ'' is a metastable phase with a monoclinic structure, γ' is also metastable with a b.c.c. structure, and γ precipitated have an equilibrium b.c.c. structure [10].

Furthermore, it has been shown that the GP zones are not the least stable of the metastable phases in the Cu–Be system, since at room temperature equiaxed Be-enriched zones have been observed to precede their formation [10–14]. Moreover, the precipitation process in these alloys can be regarded [15] as an isostructural decomposition of the f.c.c. phase into Be-rich and Be-depleted regions, followed by transformation of the Be-enriched f.c.c. regions into Be-enriched b.c.c. regions via Bain strain in concomitance with atomic order to form the B_2 structure. The morphology and structure of the γ'' and γ' phases are interpreted as constrained states of the same precipitated Be phase γ with different habit planes [15]. In line with these results, it has also been suggested recently [16, 17] that GP zones and γ'' are γ' considered to transform continuously to the following phase during isothermal aging treatment.

The above precipitation sequence has been extensively studied, with a wide variety of interpretations regarding morphology, crystallography and habit planes of the several intermediate phases formed prior to the equilibrium γ phase. In addition to continuous precipitation, cells of discontinuous precipitation advance from grain boundaries into grain center regions where continuous precipitation occurred [18–20]. The precipitation sequence for simultaneous continuous and discontinuous modes, recently studied [21], is sensitive to heat treatment. For instance the γ'' phase is absent from a directly quenched (to 623 and 673 K) and aged Cu–2Be alloy [10]. Experimental work to date has predominantly been done under isothermal conditions and little literature exists regarding the non-isothermal precipitation stages [16, 22, 23].

On the other hand, when a second solute X which interacts with vacancies but does not migrate to the hardening zones is added to a precipitation hardening binary alloy, the X atoms will form traps for vacancies and may reduce the rate of clustering of the zone-forming beryllium atoms by starving them of vacancies.

This paper studies the influence of the heating rate on the precipitation effects in a quenched Cu–2Be–0.2Mg alloy. Its main objectives are: a) to discriminate the non-isothermal precipitation sequence by using enthalpimetric calculations; b) to evaluate the different precipitation stages as a function of heating rate; c) to elucidate the origin (nucleation and growth or transition) of these stages; and d) to provide kinetic data affording a deeper insight into the atomic mechanisms of the decomposition process.

As Be precipitation from a Cu-rich matrix involves enthalpy changes large enough to allow differential scanning calorimetry (DSC), that technique was used in this work.

Material and experimental procedure

The alloy employed in this study was prepared in a Baltzer VSG 10 vacuum induction furnace from a polycrystalline Cu–2 mass% Be alloy received as 150×150 mm square plates 1.0 mm thick, and from magnesium (purity, 99.9%). After chemical analysis, it

was found that the alloy contained 2 mass% Be and 0.2 mass% Mg. The ingot was subsequently hot-forged at 1123 K to a thickness of 20 mm, pickled with a solution of nitric acid (15%) in distilled water to remove surface oxide, annealed at 1123 K for 72 h to achieve homogeneity, and cooled in the furnace to room temperature. The ingot was then cold-rolled to 1.0 mm thickness with intermediate anneals at 1123 K for 1 h. Microcalorimetric analysis of the samples was performed in a DuPont 2000 thermal analyzer. Specimen discs 1.0 mm thick and 6 mm in diameter were prepared by using a spark-cutter machine. The samples were solubilized at 1073 K during 3 h, water-quenched and stored at room temperature for 2 h prior to DSC measurements of the heat flow by operating the calorimeter in the constant-heating mode (heating rates of 1.50, 1.33, 0.83, 0.50, 0.33, 0.167, 0.082 and 0.033 K s^{-1}). To increase measurement sensitivity, a high-purity and well-annealed copper disc with mass approximately equal to that of the sample and in which no thermal events occur over the temperature range scanned, was used as a reference in each case. Both reference and specimen were enclosed in an aluminium pan sealed with an aluminium cover. To minimize oxidation, dried nitrogen was passed through the calorimeter ($0.8 \cdot 10^{-4}$ m^3 min^{-1}).

Runs were recorded between 300 and 880 K. Beyond approximately 800 K (depending on the heating rate), only heat effects corresponding to dissolution were observed in the DSC traces, and in this precipitation study, therefore, only the 300–800 K interval was analyzed. After the first run, each specimen was maintained at 880 K for 5 min and allowed to cool freely in the calorimeter for 3 h, yielding cooling curves that were very similar and nearly exponential. It was observed that the cooling rate was 0.417 K s^{-1} at 880 K, and 0.117 K s^{-1} below 560 K. When room temperature was reached, a second run at the same heating rate was made on each specimen. The DSC traces presented in this work were obtained by subtracting the baseline from the first run. This baseline represents the temperature-dependent heat capacity of the alloy under the existing thermal conditions; its value was in agreement with the Kopp–Neumann rule. Afterwards, the resulting traces were converted into a differential-heat-capacity *vs*. temperature curve. The heat-capacity remainder, i.e. the differential heat capacity, ΔC_p, is the heat associated with solid-state reactions during the DSC run. Thus, reaction peaks in the ΔC_p *vs. T* curve can be characterized by the reaction enthalpy of a particular event. The DSC curves presented in this work are always such rerun-corrected curves.

Results and discussion

DSC curves

Figure 1 shows DSC runs at heating rates ϕ. Since no exothermic heat flow occurs during a second run, this means that, after the first run, precipitation proceeds completely during cooling. Thus, the curves obtained by subtracting the second run from the first one reflect only the heat flow difference due to the free enthalpy difference just before the runs. The DSC traces show two main effects, A and B, comprising subeffects A_1 and A_2 and B_1 and B_2, respectively. Just before the first run, in all traces

the heat flow is higher than before the second run (the matrix of a quenched specimen is supersaturated); accordingly, the four subeffects observed in the rerun-corrected curves will be generally exothermic. Hence, the exothermic effects A_1, A_2, B_1 and B_2 are interpreted as follows: Effect A_1 is related to GP zone formation, while effect A_2 is related to γ'' phase precipitation. Effect B_1 is associated with GP zone and γ'' phase transformations to a state with γ' precipitates; effect B_2 is associated with γ'' and γ' phase transformations into the γ phase. These interpretations will be discussed in a later section. As the DSC heating rate was increased, the effects shifted to higher temperatures, effects A_1 and B_1 tended to disappear, the prevailing thermal events then corresponding to A_2 and B_2. Additionally, there was an overlapping of events A_1 and A_2 and of B_1 and B_2 at all heating rates.

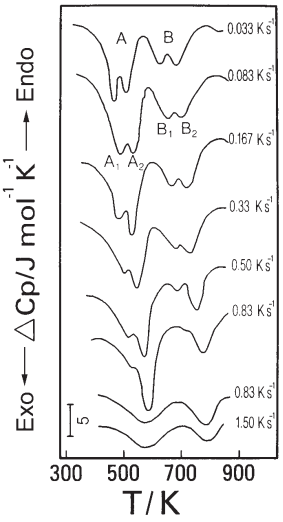

Fig. 1 DSC traces for quenched Cu–2Be–0.2Mg. Heating rates ϕ and two main effects A and B (comprising subeffects A_1 and A_2 and B_1 and B_2) are shown

All heat contents were determined by measuring the area between the rerun-corrected DSC curves. In the case of overlapping effects A_1 and A_2, and B_1 and B_2, the respective heat contents were obtained by a deconvolution process based on a heat flow extrapolation of effects A_1 and A_2, and B_1 and B_2 at the temperatures at which these effects coexisted. It is worth recalling that the end-temperature ranges of these effects lie within those of the GP zones and γ'', γ' and γ phases, in line with literature results [7, 8, 10, 17, 19, 24] for all heating rates employed herein.

Table 1 shows the initial peak and end-temperatures T_0, T_p and T_e, respectively, together with the heat content ΔH of all peaks. It can be observed that with increasing heating rate the heat contents ΔH_{A1} and ΔH_{B1} decrease, while the heat contents ΔH_{A2} and ΔH_{B2} increase. The characteristic temperatures too increase with increasing heat-

Table 1 Initial, peak and end temperatures of effects A_1, A_2, B_1 and B_2 and respective heat contents in quenched Cu–2Be–0.2Mg as a function of differential scanning calorimetry heating rate ϕ. Values for heat contents ΔH_A and ΔH_B are also given

Thermal event	T/K ΔH/J mol^{-1}	ϕ/K s^{-1}							
		0.033	0.083	0.167	0.333	0.50	0.833	1.333	1.5
A_1	T_0	328	336	344	360	374	394	–	–
	T_p	464	478	490	508	518	528	–	–
(GP)	T_e	518	546	530	552	581	589	–	–
	$-\Delta H_{A1}$	618	600	565	540	488	357	–	–
A_2	T_0	443	471	480	488	495	500	–	–
	T_p	506	524	534	554	569	582	–	–
	T_e	562	580	600	625	645	670	695	700
(γ'')	$-\Delta H_{A2}$	535	540	554	562	571	607	623	561
	$-\Delta H_A$	1153	1140	1119	1102	1059	964	623	561
B_1	T_0	574	594	614	640	660	680	–	–
	T_p	629	640	659	681	693	710	–	–
(γ')	T_e	695	706	718	728	735	742	–	–
	$-\Delta H_{B1}$	374	334	313	286	235	141	–	–
B_2	T_0	638	645	650	665	682	702	–	–
	T_p	690	700	716	730	745	760	–	–
	T_e	715	725	745	770	790	820	825	830
(γ)	$-\Delta H_{B2}$	280	286	292	310	350	376	402	382
	$-\Delta H_B$	654	620	605	596	585	517	402	382

ing rate. Further, ΔH_A and ΔH_B for composite peaks always decrease with increasing heating rate. The interplay of thermal events A_1 and A_2 is such that A_1 decreases as A_2 increases with the heating rate, so that combined precipitation of GP zones and γ'' takes place at low and medium heating rates. With increasing heating rates, the amount of GP zones precipitated decreases, but for precipitation to proceed, an increased amount of γ'' nucleates and grows. GP zone formation becomes less important (even disappearing) as the heating rate is increased, because the rate of annihilation of excess vacancies at these heating rates must be much larger than the maximum annihilation rates compatible with GP zone formation. Since the heat contents of thermal effects A_1 and A_2 vary inversely, GP and γ'' nucleate independently. As shown in later sections, the decrease in the heat content of effect B_1 associated with γ' is related to the decrease in heat content of the GP zones when the heating rate is increased. At low and high temperatures, global heat events ΔH_A and ΔH_B decrease with increasing heating rate, because they exhibit heat effects (composites in this case) normally observed in non-isothermal precipitation phenomena [25]. That is, as precipitation reactions are usually controlled by diffusion, an increased DSC heating rate results in increases in precipitation temperatures and causes a two-fold effect: (1) the number of atoms precipitated decreases due to increased solid solubilities at the increased precipitation temperatures; and (2) the proportion of phases stable at high temperatures in the precipitating phases increases.

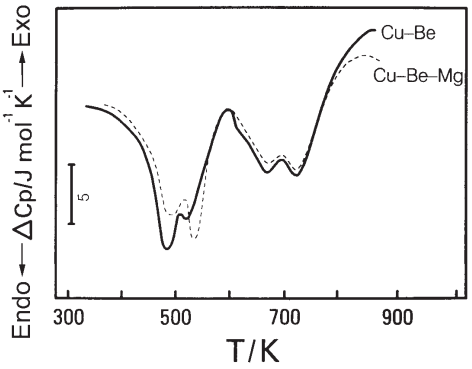

Fig. 2 DSC curves for quenched Cu–2Be and Cu–2Be–0.2Mg at a heating rate of 0.167 K s^{-1}

Figure 2 shows DSC traces on heating at 0.167 K s^{-1} for Cu–2Be and Cu–2Be–0.2Mg. Comparison of the curves shows that magnesium addition reduces the amount and rate of GP zone formation. This behaviour can be attributed to the strong interaction between Mg atoms and vacancies. Due to the strong influence of solute-vacancy pairs on the rate and amount of GP and γ'' formation, their presence will be considered in more detail. In fact, vacancy-Mg binding in the present alloy is important as regards the effective vacancy mobility. In general, the binding effect arises from two factors: a size factor and an electronic factor [26]. The size factor is responsible for

the strain field produced by the size mismatch for oversized solute elements such that the lattice strain produced is minimized by vacancy–solute atom association. The electronic factor, in contrast, is considered to be prevalent in the presence of solute atoms with valence higher than that of the host element. When magnesium is added to copper as the host element, both factors are present, taking Cu with unitary valence. If the activation energy for vacancy formation in a dilute Cu–Mg alloy is regarded as $E_f=E_{sd}/2$, E_{sd} being the activation energy for self-diffusion, which is estimated from the Brown and Ashby correlations [27], then E_f=98.6 kJ mol^{-1}. Assuming that for pure copper the energy for vacancy formation is E_v^f=106.4 kJ mol^{-1} [28], substitution of E_f [29] leads to

$$E_f = E_v^f - E_{v-s}\left\{\frac{1-12c}{12c}\exp\left(-\frac{E_{v-s}}{RT_q}\right)+1\right\}^{-1} \quad (1)$$

where T_q is the quenching temperature and c is the solute concentration.

The iteratively calculated value of E_{v-s} for quenching from 1073 K is 0.25 eV. Such a value is considered high enough for an important fraction of atoms to be bound [30]. The effect of vacancy trapping by solute atoms may be important with respect to their thermal release in determining the bound vacancy concentration. Assuming that $E_{v-s}=5RT$ [31] in the present case gives $T\leq 570$ K, which means that the trapping effect is effectively important in the range of temperatures of GP zone formation.

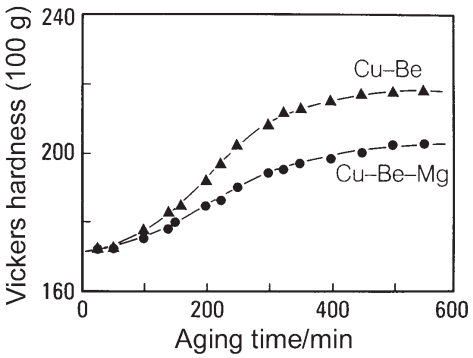

Fig. 3 Microhardness *vs*. time of aging at 423 K

The former considerations can be observed in Fig. 3, where the Vickers microhardening is plotted *vs*. time for an aging temperature of 423 K, for both Cu–2Be and Cu–2Be–0.2Mg alloys. This Figure shows that the hardening rate of GP zone formation is decreased by the presence of magnesium.

On the other hand, the small knee observed in Fig. 2 at the beginning of the peak associated with the transition to γ' phases, present for the alloy not containing Mg, and attributed to discontinuous precipitation [32], is absent for the alloy containing Mg. This fact strongly suggests that discontinuous precipitation is inhibited by magnesium addition.

Precipitation phenomena observed for effect A

It is thought that effect A can be understood as a result of the combined precipitation of GP and γ″. To identify such events, theoretical calculation of the heat evolution during the precipitation of GP zones and γ″ separately is required, assuming that at the end-temperatures of effects A_1 and A_2 no precipitation of the respective phases is taking place; i.e. the composition of the Cu-rich matrix is given by the solid solubilities for the GP zones and the γ″ phase at the end of each thermal effect [25, 33]: $c_M^{GP}(T_e^{GP})$ and $c_M^{\gamma''}(T_e^{\gamma''})$. This is equivalent to the existence of a dynamic equilibrium state for the phase at the end-temperature [34–36]. It also assumed that the magnesium atoms do not participate in the precipitation process [37].

The total precipitation heat for the GP zones and γ″ can be calculated separately by considering (a) the precipitated Be atoms in the GP zones and the γ″ phase, and (b) their respective heats of precipitation, as follows. For the GP zones after precipitation, the mole fraction of the Cu-rich matrix is given by $c_M^{GP}(T_e^{GP})$, and the precipitation reaction is then

$$Cu_{[1-c]}Be_{[c]} \rightarrow mCu_{[1-c_M^{GP}(T_e^{GP})]} + Be_{[c_M(T_e^{GP})]} + pBe \tag{2}$$

where m and p are the numbers of moles of Cu-rich phase and GP zones, respectively, the latter being considered as a first approximation to be formed by Be plates [10, 15], while c is the initial Be concentration of the alloy.

Conservation of mass for copper requires

$$1-c=m[1-c_M^{GP}(T_e^{GP})] \Rightarrow m=\frac{1-c}{1-c_M^{GP}(T_e^{GP})} \tag{3}$$

and for beryllium:

$$c=mc_M^{GP}(T_e^{GP})+p \tag{4}$$

From Eqs (3) and (4):

$$p=\frac{c-c_M^{GP}(T_e^{GP})}{1-c_M^{GP}(T_e^{GP})} \tag{5}$$

Similarly, for γ″ precipitation:

$$Cu_{(1-c)}Be_c \rightarrow rCu_{[1-c_M^{\gamma''}(T_e^{\gamma''})]}Be_{[c_M^{\gamma''}(T_e^{\gamma''})]} + qCuBe \tag{6}$$

where the γ″ composition was taken as CuBe [15], although it varies somewhat with temperature [22]; r is the number of moles of the Cu-rich matrix and q that of the CuBe γ″ phase. Conservation of mass for copper requires

$$1-c=r[1-c_M^{\gamma''}(T_e^{\gamma''})]+q \tag{7}$$

and for beryllium:

$$c=rc_M^{\gamma''}(T_e^{\gamma''})+q \tag{8}$$

From Eqs (7) and (8):

$$r=\frac{1-c}{1-2c_{\mathrm{M}}^{\gamma''}(T_{\mathrm{e}}^{\gamma''})} \tag{9}$$

$$q=\frac{c-c_{\mathrm{M}}^{\gamma''}(T_{\mathrm{e}}^{\gamma''})}{1-2c_{\mathrm{M}}^{\gamma''}(T_{\mathrm{e}}^{\gamma''})} \tag{10}$$

Since $1>>2c_{\mathrm{M}}^{\gamma''}(T_{\mathrm{e}}^{\gamma''})$, the denominators in Eqs (2), (5), (9) and (10) can be approximated to unity. The values of $c_{\mathrm{M}}^{\mathrm{GP}}(T_{\mathrm{e}}^{\mathrm{GP}})$ and $c_{\mathrm{M}}^{\gamma''}(T_{\mathrm{e}}^{\gamma''})$ in Eqs (5) and (10) were obtained from the solubility curves reported by Strutt and Williams [26]. For above-mentioned consideration (b), the values of the GP and γ″ precipitation heats can be obtained from the slope of the straight line through the data points of the plot of the logarithm of (metastable) solid solubility *vs*. reciprocal temperature [38]. Table 2 lists precipitation heat values obtained from the compilation of data points in [24], where values for γ′ and γ are included.

Table 2 Precipitation heats of GP zones, stable and metastable phases in Cu–Be–Mg alloys, calculated from [26]

Phase/zone	Precipitation heat/kJ mol^{-1} Be
GP	18.71
γ″	28.08
γ′	34.13
γ	37.72

Therefore, the heat $\Delta H_{\mathrm{c}}^{\mathrm{GP}}$ produced during GP precipitation is

$$\Delta H_{\mathrm{c}}^{\mathrm{GP}}=\Delta H_{\mathrm{p}}^{\mathrm{GP}}[c-c_{\mathrm{M}}^{\mathrm{GP}}(T_{\mathrm{e}}^{\mathrm{GP}})] \tag{11}$$

where $\Delta H_{\mathrm{p}}^{\mathrm{GP}}$ is the precipitation heat for the GP zones. For γ″ the total precipitation heat $\Delta H_{\mathrm{c}}^{\gamma''}$ per mole alloy is

$$\Delta H_{\mathrm{c}}^{\gamma''}=\Delta H_{\mathrm{p}}^{\gamma''}[c-c_{\mathrm{M}}^{\gamma''}(T_{\mathrm{e}}^{\gamma''})] \tag{12}$$

where $\Delta H_{\mathrm{p}}^{\gamma''}$ is the precipitation heat for the γ″ phase.

Figure 4 gives the calculated estimates for $\Delta H_{\mathrm{c}}^{\mathrm{GP}}$ and $\Delta H_{\mathrm{c}}^{\gamma''}$ and the experimental values for the heat content $\Delta H_{\mathrm{e}}^{(\mathrm{GP}+\gamma'')}$ of effect A, as a function of the heating rate ϕ. It can be seen that the calculated values for γ″ precipitation are larger than for those for GP zone precipitation, because (1) the precipitation heat of the γ″ phase is larger than that of the GP zones, and (2) beryllium atoms in γ″ phase precipitation outnumber the beryllium atoms in GP zone precipitation. Figure 4 shows that the measured values of the heat content of effect A, always lie between the limits calculated for GP and γ″ precipitation. At low heating rates, the experimental heat contents indicate enhanced GP precipitation. For high DSC heating rates, the experimental values correspond fairly well to predominant γ″ formation, and thus beryllium precipitation then pro-

ceeds mainly as γ″ phase precipitation. Calculated values of event A which take into account the relative experimental importance of event A_1 and A_2 separately can be obtained by computing a combined precipitation heat defined as follows:

$$\Delta H_c^{(GP+\gamma'')} = \psi \Delta H_c^{GP} + (1-\psi)\Delta H_c^{\gamma''} \tag{13}$$

where the strengthening factor ψ is

$$\psi = \frac{\Delta H_e^{GP}}{\Delta H_e^{GP} + \Delta H_e^{\gamma''}} \tag{14}$$

where ΔH_e^{GP} and $\Delta H_e^{\gamma''}$ are the heat contents of deconvoluted thermal effects A_1 and A_2, respectively.

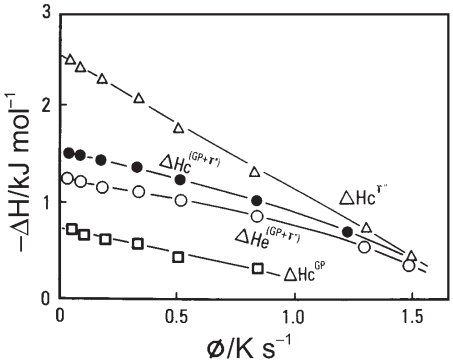

Fig. 4 Heat content $\Delta H_e^{(GP+\gamma'')}$ of effect A for quenched Cu–2Be–0.2Mg as a function of the DSC heating rate. The calculated curves ΔH_c^{GP}, $\Delta H_c^{\gamma''}$ and $\Delta H_c^{(GP+\gamma'')}$ are also shown

The factor ψ is a function of the heating rate. The experimental and calculated plots are in fairly good agreement in Fig. 4. It is worth noting that for the GP zones, the interfacial energy and the energy related to the elastic strains can have a significant influence on the total energy of formation of the zones [39]. Since the creation of strains and of interfaces requires an energy input into the specimen, both strain and interfacial energy reduce the total amount of energy associated with the formation of zones. The importance of these contributions is determined by the average size of the zones: the total energy of formation of small zones contains relatively large strain and interfacial energy contributions.

The above analysis leads to the conclusion that heat event A corresponds to an overlapping sequential precipitation of GP zones and γ″ phase, where both nucleate and grow independently.

The matrix compositions c_M for the different phases, shown in Fig. 5, were obtained from [24].

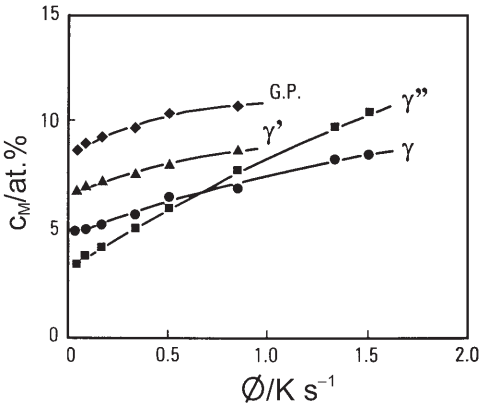

Fig. 5 Matrix composition for GP zones and γ″, γ′ and γ phases

Precipitation phenomena observed for effect B

As no endothermic effects occur during the DSC runs, no dissolution of GP zones and γ″ takes place. Hence, the thermal events B_1 associated with γ′ and B_2 associated with stable phase γ, cannot correspond to nucleation and growth processes, but rather to transitions. In fact, if the procedure outlined in the previous section in order to verify the nature of effects A_1 and A_2 is now applied to events B_1 and B_2, then the experimentally measured heats $\Delta H_e^{(\gamma'+\gamma)}$ are always outside the calculated boundaries of γ′ and γ precipitation for all heating rates and are far below the calculated heats $\Delta H_e^{(\gamma'+\gamma)}$. This feature is shown in Fig. 6. Thus, it must be concluded that exothermic effect B should be attributed to transitions of less stable phases to the γ′ and γ phases.

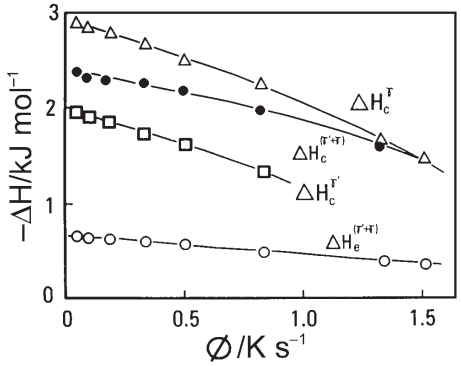

Fig. 6 Experimental heat content $\Delta H_e^{(\gamma'+\gamma)}$ of effect B for quenched Cu–2Be–0.2Mg as a function of the DSC heating rate. Calculated curves $\Delta H_c^{\gamma'}$, ΔH_c^{γ} and $\Delta H_c^{(\gamma'+\gamma)}$ for γ′, γ and combined γ′, γ precipitation are also shown. Note that the experimental curve is outside the γ′ and γ calculated boundaries

The next task is to identify the phase or phases transformed from their primitive state into the γ′ and γ phases, and their relative contributions to such transitions. To this end, it is first required to calculate the heat evolved in the transition from a less stable to a more stable phase. For all the possible transitions considered, the heat contents are

$$\Delta H_c^{GP-\gamma'} = (\Delta H_p^{\gamma'} - \Delta H_p^{GP})[c - c_M^{GP}(T_e^{GP})] \quad (15)$$

$$\Delta H_c^{\gamma''-\gamma'} = (\Delta H_p^{\gamma'} - \Delta H_p^{\gamma''})[c - c_M^{\gamma''}(T_e^{\gamma''})] \quad (16)$$

$$\Delta H_c^{\gamma''-\gamma} = (\Delta H_p^{\gamma} - \Delta H_p^{\gamma''})[c - c_M^{\gamma''}(T_e^{\gamma''})] \quad (17)$$

$$\Delta H_c^{\gamma'-\gamma} = (\Delta H_p^{\gamma} - \Delta H_p^{\gamma'})[c - c_M^{\gamma'}(T_e^{\gamma'})] \quad (18)$$

where $\Delta H_c^{GP-\gamma'}$, $\Delta H_c^{\gamma''-\gamma'}$, $\Delta H_c^{\gamma''-\gamma}$ and $\Delta H_c^{\gamma'-\gamma}$ are the heats amounts evolved during the transitions GP→γ′, γ″→γ′, γ″→γ and γ′→γ, respectively.

The transition GP→γ was not considered, since it leads to irrelevant results. All other terms of Eqs (17)–(20) have already been defined. If the calculated heats $\Delta H_c^{GP-\gamma'}$ and $\Delta H_c^{\gamma''-\gamma'}$ are plotted as a function of the heating rate and are compared with the experimental value $\Delta H_e^{\gamma'}$ measured after deconvolution of the thermal effect B_1 shown in Fig. 7.

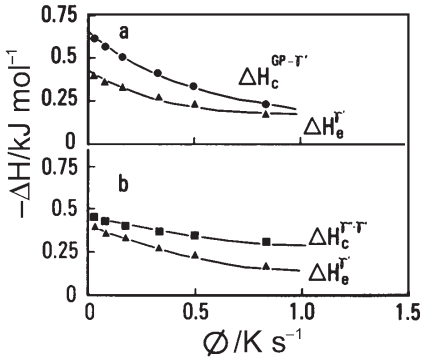

Fig. 7 Heat $\Delta H_e^{\gamma'}$ evolved during the transition to the state with the γ′ phase as a function of the DSC heating rate. The calculated values $\Delta H_c^{GP-\gamma'}$ and $\Delta H_c^{\gamma''-\gamma'}$ for the heat evolved during the transitions GP→γ′ and γ″→γ′ are also shown in (a) and (b)

It can be seen in Fig. 7(a) that the transition GP→γ′ tends to be possible only at high heating rates, while the contrary holds for the transition γ″→γ′ shown in Fig. 7(b). In fact, both heat effects associated with GP and γ′ (Fig. 1) decrease with increasing heating rate. Accordingly, it is believed that both the GP zones and the γ″ phase contribute to the state with beryllium precipitated as the γ′ phase. This is not surprising as far as the GP zones are concerned, because the possibility of γ′ formation being inherited from GP zones has been experimentally observed and theoretically analyzed, particularly when the zones have no chance to coarsen and begin to transform into γ″ [10]. This might also explain why the transition GP→γ″ is possible only at very low heating rates, as shown in Fig. 8,

where $\Delta H_c^{GP-\gamma''}$ and $\Delta H_e^{\gamma''}$ are plotted as a function of ϕ. It can be observed that $\Delta H_c^{GP-\gamma''} \approx \Delta H_e^{\gamma''}$ for heating rates lower than 0.1 K s^{-1}.

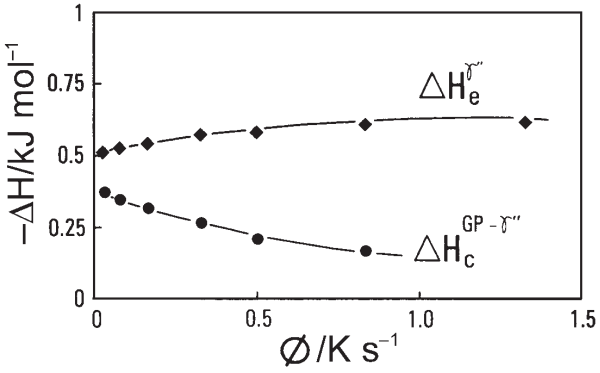

Fig. 8 Heat $\Delta H_e^{\gamma''}$ evolved during γ'' phase precipitation as a function of the heating rate. The calculated heat content curve $\Delta H_c^{GP-\gamma''}$ for the transition GP→γ'' is also shown. Note that the γ'' phase can be inherited from GP zones only at very low DSC heating rates

Figures 9(a) and 9(b) depict the calculated values of $\Delta H_c^{\gamma''-\gamma}$ and $\Delta H_c^{\gamma'-\gamma}$ and the experimental values for ΔH_e^{γ}. At high heating rates, the $\gamma''\rightarrow\gamma$ transition takes place (Fig. 9a). This feature is in agreement with an absence of GP zones and γ' for these high values of ϕ, as was shown in Fig. 1; thus, such a mode of transition is the only one possible. At very low heating rates γ stems from the transition $\gamma'\rightarrow\gamma$, as observed in Fig. 9b. The above results suggest that γ'' is partially involved in two of the observed transitions, and thus it can be assumed that the transitions GP, $\gamma''\rightarrow\gamma'$ and γ'', $\gamma'\rightarrow\gamma$ take place. They require that the heat effect associated with γ'' be partitioned into a fraction α contributing to the transition to the γ' phase state, and a fraction

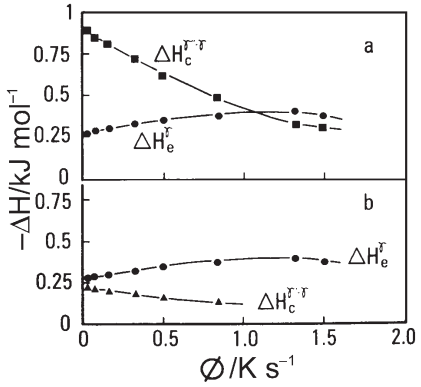

Fig. 9 Heat evolved during the transition to the state with the γ phase as a function of the DSC heating rate. The calculated values $\Delta H_c^{\gamma''-\gamma}$ and $\Delta H_c^{\gamma'-\gamma}$ of the heat content curves for the transitions $\gamma''\rightarrow\gamma$ and $\gamma'\rightarrow\gamma$ are also shown in (a) and (b)

(1–α) contributing to the transition to the γ phase state. As the heat evolved in each thermal event in the DSC traces corresponds to a certain amount of the phase associated with the event, strengthening factors can be defined as follows:

$$\psi^* = \frac{\Delta H_e^{GP}}{\Delta H_e^{GP} + \alpha \Delta H_e^{\gamma''}} \tag{19}$$

and

$$\Psi^* = \frac{(1-\alpha)\Delta H_e^{\gamma''}}{(1-\alpha)\Delta H_e^{\gamma''} + \Delta H_e^{\gamma}} \tag{20}$$

and they ponderate the calculated heats of transition $\Delta H_c^{\gamma'}$ and ΔH_c^{γ} involved in achieving the states γ′ and γ. By equating $\Delta H_c^{\gamma'} = \Delta H_e^{\gamma'}$ and $\Delta H_c^{\gamma} = \Delta H_e^{\gamma}$, the following expressions for such transitions can be written

$$\Delta H_e^{\gamma'} = \psi^* \Delta H_{GP}^{\gamma'} [c - c_M^{GP}(T_e^{GP})] + (1-\psi^*) \Delta H_{\gamma''}^{\gamma'} [c - c_M^{\gamma''}(T_e^{\gamma''})] \tag{21}$$

and

$$\Delta H_e^{\gamma} = \Psi^* \Delta H_{\gamma''}^{\gamma'} [c - c_M^{\gamma''}(T_e^{\gamma''})] + (1-\Psi^*) \Delta H_{\gamma'}^{\gamma} [c - c_M^{\gamma'}(T_e^{\gamma'})] \tag{22}$$

where

$$\Delta H_{GP}^{\gamma'} = \Delta H_p^{\gamma'} - \Delta H_p^{GP};\ \Delta H_{\gamma''}^{\gamma'} = \Delta H_p^{\gamma'} - \Delta H_p^{\gamma''};\ \Delta H_{\gamma''}^{\gamma'} = \Delta H_p^{\gamma'} - \Delta H_p^{\gamma''} \text{ and}$$
$$\Delta H_{\gamma'}^{\gamma} = \Delta H_p^{\gamma} - \Delta H_p^{\gamma'}.$$

Values for ψ^* and Ψ^* are obtained from Eqs (21) and (22) and are plotted as a function of ϕ in Fig. 10, and finally values for $\alpha(\psi^*)$ and $\alpha(\Psi^*)$ are shown in Fig. 11. It can be observed that $\alpha(\psi^*) = \alpha(\Psi^*)$ for all heating rates employed, thereby confirming that the transitions formulated in Eqs (21) and (22) are correct.

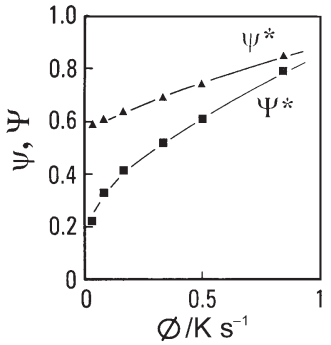

Fig. 10 Calculated factors ψ^* and Ψ^* from Eqs (21) and (22) as a function of the DSC heating rate

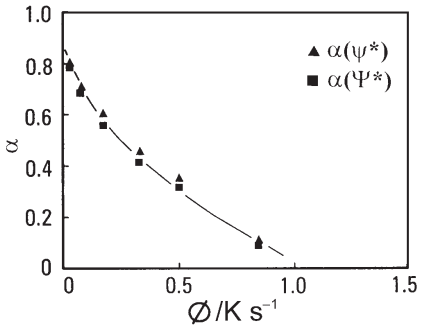

Fig. 11 Values for $\alpha(\psi^*)$ and $\alpha(\Psi^*)$ computed from Eqs (19) and (20) as a function of the DSC heating rate

In closing this section, it is important to remark that magnesium addition can strongly suppress discontinuous precipitation, as evidenced by the absence of the knee at the beginning of the γ′ transition peak in Cu–2Be [32] and as also reported from metallographic studies [37].

Activation energy analysis

Activation energies for thermal events associated with the formation of GP zones and γ″ and those for γ′ and γ phase transformations were obtained by employing a variant of the Kissinger analysis [40], from the slope of the straight line through the data points of the $\ln(\phi/T_f^2)$ *vs.* $1/T_f$ plot at certain transformation stages of the deconvoluted peaks, T_f being the temperature for a fixed stage of transformation. Effective activation energies were calculated at four chosen transformation stages: at peak temperature, at 10, at 50 and at 90% of the total heat evolved by effects A_1, A_2, B_1 and B_2. The values thus obtained did not differ significantly in any case. The average computed values were as follows:

$$E_a^{GP} = 1.16 \pm 0.08 \text{ eV}$$

$$E_a^{\gamma''} = 1.18 \pm 0.07 \text{ eV}$$

$$E_a^{\gamma'} = 1.37 \pm 0.08 \text{ eV}$$

$$E_a^{\gamma} = 1.74 \pm 0.09 \text{ eV}$$

where E_a^{GP}, $E_a^{\gamma''}$, $E_a^{\gamma'}$ and E_a^{γ} correspond to the GP zones and the γ″, γ′ and γ phases.

It can be observed that the E_a^{GP} value is higher than that of vacancy migration, E_m=0.99 eV (taken as about one half of 1.99 eV, the activation energy for beryllium diffusion in copper [23]) and lower than the limiting value for solute–vacancy pair dissociation, taken as E_m+E_{v-s}=1.245 eV. Therefore, the effective activation energy for GP formation, E_a^{GP}, is some weighted average value between that for monovacancies and the actual value for solute–vacancy pair migration, thus confirming that GP formation is controlled by the type of migration of defects. The same arguments hold

for γ″ formation, since thermal release becomes more important than the effect of vacancy trapping by solute atoms for $T>E_{v-s}/5R$ [31], i.e. $T>570$ K, at which the γ″ formation peak ends.

The other values of effective activation energies associated with the overall kinetics of γ′ and γ are lower than the activation energy for beryllium diffusion in copper. As such diffusion can only proceed via a vacancy mechanism, significant amounts of excess point defects are still present in all these specimens.

Another reason for the lower values of activation energies as compared with those of beryllium diffusion is that such overall values are weighted averages of activation energies controlling the kinetics of thickening and lengthening of γ′ and γ plates. Although no specific data were found for Cu–Be alloys as concerns the above differences, at least in Al–Cu alloys the rate-dependent step for thickening appeared to be ledge formation of the broad surfaces of θ′ plates, whereas the rate-dependent step for lengthening was found to be pipe diffusion. The activation energy for thickening was larger than that for lengthening [41], but slightly lower than the activation energy for copper diffusion in aluminium [42]. If the same arguments may be applied to copper–beryllium alloys, they would strongly suggest that lengthening is more important than thickening, as the phases considered become less stable. Typical transmission electron micrographs showing γ′ and γ plates reveal this feature [21]. This can be an alternative explanation for the increasing values of activation energies ob-

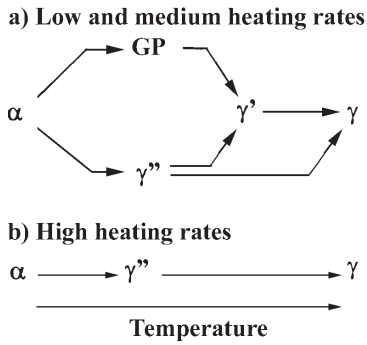

Fig. 12 Schematic representation of the phases involved at increasing temperatures in the non-isothermal precipitation in quenched Cu–2–Be–0.2–Mg

tained as the phases become more stable (γ′ and γ).

To summarize, the non-isothermal precipitation sequence in Cu–2Be–0.2Mg is schematically shown in Fig. 12.

Conclusions

Quenched Cu–2Be–0.2Mg alloys subjected to non-isothermal DSC runs using a wide range of heating rates led to the following conclusions.

The main effects of magnesium addition are to reduce the amount and rate of GP zone formation, to enhance the amount and rate of γ″ precipitation and to inhibit discontinuous γ′ and γ precipitation. At low heating rates, GP zones and the γ″ phase nucleate and grow independently. The amount of GP zones decreases with increasing heating rate and is even hindered at high heating rates, due to the inefficiency of excess vacancies. Further, the heat content of the combined GP/γ″-phase precipitation effect appeared to be proportional to the number of beryllium atoms precipitated yielding an average value for the heat of beryllium precipitation of 21 kJ mol^{-1} beryllium.

On the other hand, the γ″ phase can by inherited from GP zones only at very low heating rates. Additionally, the γ″ phase contributes partially to the transitions to states with the γ′ and γ phases, while transition to the state with the γ′ phase arises from the combined contribution of GP zones and γ″, and transition to the state with the γ phase arises from the combined contribution of the γ″ and γ′ phases. At the highest heating rates, the state with the γ′ phase is absent and transition to the state with the γ phase arises completely from the γ″ phase.

The effective activation energies of GP zone and γ″ formation are consistent with weighted average values for vacancy and solute–vacancy complex migration. The effective activation energies associated with the γ′ and γ phases display increasing values. Two factors can influence this feature: the mobility of dissolved atoms assisted by residual excess vacancies and the growth direction (either normal or perpendicular to the plates). The relative importance of these factors may depend on temperature.

* * *

The authors would like to thank the Fondo Nacional de Desarrollo Científico y Tecnológico (Fondecyt), Project No. 1980731, for financial support, and the Instituto de Investigaciones y Ensayes de Materiales (Idiem), Universidad de Chile, for the facilities provided for this research work.

References

1 Z. Trojanová, V. Gröger, J. Stelzhammer and G. Bischof, Mater. Sci. Eng. A, 234–236 (1997) 449.
2 Z. Trojanová, V. Gröger and J. Stelzhammer, Phys. Status Solidi A, 157 (1996) 295.
3 Young-Gab Chun and Su-Il Pyun, Mater. Sci. Eng. A, 206 (1996) 49.
4 R. Koch, Phil. Mag. A, 68 (1993) 1045.
5 C. R. Houska, J. Mater. Sci., 29 (1994) 4447.
6 V. Gröger, P. Fratzl, W. Oahl, O. Paris, G. Bischof and G. Krexner, Acta Metall., 43 (1995) 1305.
7 K. Shimizu, Y. Mikami, H. Mitani and K. Otzuka, Trans. Jpn. Inst. Met., 12 (1971) 206.
8 S. Yamamoto, M. Matsui and Y. Murakami, Trans. Jpn. Inst. Met., 12 (1971) 159.
9 W. H. Bonfield and B. C. Edwards, J. Mater. Sci., 9 (1974) 398.
10 R. J. Rioja and D. E. Laughlin, Acta Metall., 28 (1980) 1301.
11 J. M. Pelletier, G. Vigier, C. Mai and R. Borrelly, Acta Metall., 31 (1983) 1491.
12 Y. M. Koo, J. B. Cohen, S. M. Shapiro and L. E. Tanner, Acta Metall., 36 (1988) 591.
13 Y. M. Koo and J. B. Cohen, Acta Metall., 37 (1989) 1295.

14 J. B. Cohen, Metall. Trans., 23A (1992) 2685.
15 A. G. Khachaturyan and D. E. Laughlin, Acta Metall. Mater., 38 (1990) 1823.
16 A. Yamamoto, R. Nozato, T. Morimoto and H. Tsubakino, Mater. Trans. JIM, 34 (1993) 312.
17 A. Yamamoto and H. Tsubakino, Scripta Metall. Mater., 31 (1994) 787.
18 W. Bonfield and B. C. Edwards, J. Mater. Sci., 9 (1974) 409.
19 T. Tsubakino, R. Nozato and H. Hagiwara, Trans. Jpn. Inst. Met., 22 (1981) 153.
20 H. Tsubakino, R. Nozato and A. Yamamoto, J. Mater. Sci., 26 (1991) 2851.
21 H. Tsubakino, R. Nozato and A. Yamamoto, Mater. Sci. Tech., 9 (1993) 288.
22 L. G. Garrilenko, B. M. Mogutnov and L. A. Shvartsman, Phys. Met. Metall., 27 (1969) 116.
23 T. Ohshima and K. Hirano, Thermochim. Acta, 93 (1985) 645.
24 A. J. Strutt and D. B. Williams, Philos. Mag., 67A (1993) 1007.
25 M. J. Starnik and P. Van Mourik, Metall. Trans., 22A (1991) 665.
26 A. K. Mukhophyay, G. J. Shiflet and E. A. Starke, Scr. Metall. Mater., 24 (1990) 307.
27 A. M. Brown and M. F. Ashby, Acta Metall., 28 (1980) 1085.
28 H. Kimura and R. Maddin, Quench Hardening in Metals, North-Holland, Amsterdam 1971, p. 17.
29 J. I. Takamura, M. Doyama and H. Kisitani, Point Defects and Defect Interactions in Metals, North-Holland, Amsterdam 1982, p. 452.
30 S. Özbilen and H. M. Flower, Acta Metall, 37 (1989) 2993.
31 L. K. Mansur, Acta Metall., 29 (1981) 375.
32 A. Varschavsky and E. Donoso, Thermochim. Acta, 266 (1995) 257.
33 M. J. Starnik and P. Van Mourik, Mater. Sci. Eng., A156 (1992) 183.
34 A. Varschavsky and E. Donoso, Mater. Sci. Eng., A145 (1991) 95.
35 A. Varschavsky, Thermochim. Acta, 203 (1992) 391.
36 A. Varschavsky and M. Pilleux, Mater. Letts., 17 (1993) 364.
37 Y. Wang, Y. Ling and S. Zhou, Proceedings of the Copper 91 Conference, V. I. Sections Applications, Eds. E. Gervais and A. Varschavsky, Pergamon Press, Ottawa 1991, p. 221.
38 M. van Rooyen and E. J. Mittemeijer, Metall. Trans., 20A (1989) 1207.
39 A. M. Zahra, M. Laffitte and M. Winterberger, Mem. Sci. Rev. Metall., 74 (1977) 561.
40 E. J. Mittemeijer, Liu Chang, P. J. van der Schaaf, C. M. Brakman and B. M. Korevaar, Metall. Trans., 19A (1988) 925.
41 H. I. Aaronson and C. Laird, Trans. AIME, 242 (1968) 1437.
42 L. F. Mondolfo, Aluminium Alloys: Structure and Properties, Butterworths, London 1976.